



# Rapid Generation of Kilonova Light Curves Using Conditional Variational Autoencoder

Surojit Saha<sup>1</sup> , Michael J. Williams<sup>2,5</sup> , Laurence Datrier<sup>2</sup> , Fergus Hayes<sup>2</sup> , Matt Nicholl<sup>3</sup> , Albert K. H. Kong<sup>1</sup> ,  
Martin Hendry<sup>2</sup> , IK Siong Heng<sup>2</sup> , Gavin P. Lamb<sup>4</sup> , En-Tzu Lin<sup>1</sup> , and Daniel Williams<sup>2</sup>

<sup>1</sup> Institute of Astronomy, National Tsing Hua University, Hsinchu City, Taiwan (ROC); [surojitsaha@gapp.nthu.edu.tw](mailto:surojitsaha@gapp.nthu.edu.tw), [akong@gapp.nthu.edu.tw](mailto:akong@gapp.nthu.edu.tw)

<sup>2</sup> Institute for Gravitational Research, School of Physics and Astronomy, University of Glasgow, Glasgow, UK

<sup>3</sup> Astrophysics Research Centre, School of Mathematics and Physics, Queens University Belfast, Belfast BT7 1NN, UK

<sup>4</sup> Astrophysics Research Institute, Liverpool John Moores University, IC2 Liverpool Science Park, 146 Brownlow Hill, Liverpool L3 5RF, UK

<sup>5</sup> Institute of Cosmology and Gravitation, University of Portsmouth, Portsmouth PO1 3FX, UK

Received 2023 May 6; revised 2023 October 6; accepted 2023 October 11; published 2024 January 23

## Abstract

The discovery of the optical counterpart, along with the gravitational waves (GWs) from GW170817, of the first binary neutron star merger has opened up a new era for multimessenger astrophysics. Combining the GW data with the optical counterpart, also known as AT 2017gfo and classified as a kilonova, has revealed the nature of compact binary merging systems by extracting enriched information about the total binary mass, the mass ratio, the system geometry, and the equation of state. Even though the detection of kilonovae has brought about a revolution in the domain of multimessenger astronomy, there has been only one kilonova from a GW-detected binary neutron star merger event confirmed so far, and this limits the exact understanding of the origin and propagation of the kilonova. Here, we use a conditional variational autoencoder (CVAE) trained on light-curve data from two kilonova models having different temporal lengths, and consequently, generate kilonova light curves rapidly based on physical parameters of our choice with good accuracy. Once the CVAE is trained, the timescale for light-curve generation is of the order of a few milliseconds, which is a speedup of the generation of light curves by 1000 times as compared to the simulation. The mean squared error between the generated and original light curves is typically 0.015 with a maximum of 0.08 for each set of considered physical parameters, while having a maximum of  $\approx 0.6$  error across the whole parameter space. Hence, implementing this technique provides fast and reliably accurate results.

*Unified Astronomy Thesaurus concepts:* [Neural networks \(1933\)](#); [Neutron stars \(1108\)](#); [Compact objects \(288\)](#); [Light curves \(918\)](#)

## 1. Introduction

The concomitant discovery of gravitational waves (GWs) and their optical counterpart electromagnetic waves (EMs) (Abbott et al. 2017a; Arcavi et al. 2017; Coulter et al. 2017; Lipunov et al. 2017; Soares-Santos et al. 2017; Tanvir et al. 2017; Valenti et al. 2017) from the merger of the binary neutron star GW170817 (Abbott et al. 2017b), also accompanied by a short gamma-ray burst (GRB) (Goldstein et al. 2017; Savchenko et al. 2017), has advanced the domain of multimessenger astronomy. This optical counterpart, designated as a kilonova (KN) and known as AT 2017gfo, has bolstered previous predictions of the existence of such electromagnetic transients (Li & Paczyński 1998; Rosswog et al. 1999). Prior to the discovery of GW170817, it was predicted that such an event would be accompanied by an EM counterpart, including short-duration GRBs (Eichler et al. 1989; Nakar 2007), emissions ranging from radio to X-rays pertaining to on- or off-axis afterglow (van Eerten & MacFadyen 2012; Coward et al. 2014; Fong et al. 2015; Lamb & Kobayashi 2016), and optical to near-IR emission resulting from the decay of  $r$ -process nuclei. A KN is an isotropic quasi-thermal transient that is powered by the radioactive decay, in the merger ejecta, of  $r$ -process nuclei, having luminosities of  $10^{40}$ – $10^{42}$  erg s<sup>-1</sup> (Li & Paczyński 1998; Rosswog et al. 1999; Metzger et al. 2010; Barnes & Kasen 2013). This EM

counterpart can provide deeper understanding of the merger environment and its products. When EM information is further combined with GW information, it leads to a unique platform for an extensive understanding of such binary events. KN models consist of one or more radioactive ejecta components that produce light curves peaking at different timescales and temperatures depending on the atomic mass number of the ejecta and on the luminosity. The two-component model consists of blue KN (Metzger et al. 2010; Roberts et al. 2011; Metzger & Fernández 2014) emission having a poor lanthanide fraction ( $10^{-5}$ ) in the merger ejecta peaking at a relatively early timescale and red KNe (Barnes & Kasen 2013; Kasen et al. 2013; Tanaka & Hotokezaka 2013) comprising lanthanide-rich ( $10^{-2}$ ) merger ejecta with peak values at later days. In the three-component model (Perego et al. 2017) there is an inclusion of purple KNe, which indicates the presence of a lanthanide fraction of  $10^{-3}$ . Various papers (Cowperthwaite et al. 2017; Villar et al. 2018) have provided the best-fit parameter for AT 2017gfo related to the blue, purple, and red KNe in terms of the ejecta mass, ejecta velocity, and lanthanide fraction. However, since there has been only one GW-confirmed detection of a KN from a merger of binary neutron stars, along with some possible candidates from other sources, it is difficult to understand and verify the properties of binary merging systems that emit electromagnetic radiation. An overview of the physical parameters that govern KNe has been provided by Metzger (2019).

In recent years, machine learning (ML) has been used for various data analysis and formulation techniques required in astronomy (Ball & Brunner 2010; Vander Plas et al. 2014;



Original content from this work may be used under the terms of the [Creative Commons Attribution 4.0 licence](#). Any further distribution of this work must maintain attribution to the author(s) and the title of the work, journal citation and DOI.

Shen et al. 2019; Ntampaka et al. 2021; Jones et al. 2022). There have been certain areas where the application of ML techniques has produced a remarkable result, especially when it focused on providing faster results as an alternative to existing methods (Ball 2011; Sipőcz et al. 2020). There is plenty of excellent literature available on a wide range of topics of ML application in astronomy and astrophysics (García-Jara et al. 2022; Gheller & Vazza 2022; Li et al. 2022; Sheng et al. 2022). In this paper, we incorporate a method from the ML domain known as autoencoder (Rumelhart et al. 1986), which is based on a feed-forward mechanism, to generate light curves. The primary task of an autoencoder is to encode the input into a lower-dimensional latent representation and then decode it back to data. In a feed-forward mechanism, the neural network has unidirectional processing of information. The striking feature for an autoencoder is that the encoder compresses high-dimensional input to a low-dimensional latent space and the decoder decompresses to produce results to match the input.

In this work, we regenerate KN light curves by implementing a conditional variational autoencoder (CVAE) (Kingma & Welling 2019), which is developed based on a variational autoencoder (Kingma & Welling 2013). We use this CVAE to generate light curves based on our choice of physical parameter values of the binary merging system. For the CVAE, once training has been completed, we have more flexibility to rapidly generate light curves based on the physical parameters depending on the choice of data set. Although KN data from only two models for training and producing results are used in this work, it is possible to extend the same idea for data from other models. Although the data have been produced from the model, this unique data analysis technique can not only generate light curves for parameter values that are not explicitly mentioned in the model but also replace the time-consuming and resource-draining simulations required for predicting light curves. The novelty of this technique is expressed in the fact that once the CVAE is trained on a KN model, we can generate numerous light curves for different combinations of physical parameters in a very short time. An alternative approach for such CVAE and KN work has been presented in Lukošiuėtė et al. (2022), where a different method has been studied for obtaining results. One of the fundamental differences between Lukošiuėtė et al. (2022) and our work is in using spectra rather than light curves during training. In our method, we look into the light-curve evolution with respect to different sets of physical parameters aiming to complete the process in a shorter timescale compared to that of existing simulation methods. This kind of rapid generation technique for KN light curves can be useful as a template for rapid parameter estimation of KNe.

In the following sections, we show the gradual implementation of our idea, and the results are discussed thereafter. In Section 3, we discuss the CVAE architecture implemented in our work. Section 4 puts forward differences in the data and the physical parameters used for the training and generation of KN light curves. Section 5 provides a detailed discussion of the results obtained after the implementation of the CVAE. In Section 6 we summarize our approach and present some important features of this technique. Additional results for reference are included in the appendix.

## 2. KN Models

KN emission results from the mass ejection in neutron star mergers (Freiburghaus et al. 1999; Ruffert & Janka 2001;

Hotokezaka et al. 2013; Kawaguchi et al. 2020). The properties of the ejecta such as the ejecta mass, velocity, and opacity dominate the peak luminosity and the time of the peak luminosity (Li & Paczyński 1998; Barnes & Kasen 2013; Kasen et al. 2013, 2015; Tanaka et al. 2017). This luminosity is sourced from the radioactive decay of the  $r$ -process elements synthesized in the merger. This work primarily focuses on two KN models having different physical parameters that determine the light curves. Below we provide an outline of the two models used in this work. In Kasen et al. (2017), light curves that are dependent on the peak magnitude and decay time with respect to the ejecta mass, velocity, and lanthanide fraction are provided. Quantitatively, the peak luminosity to first order is denoted by  $L \propto M_{\text{ej}}$  and the width of the light curve is  $\tau \propto (\kappa M_{\text{ej}}/v_{\text{ej}})^{1/2}$ , pointing to lanthanide-rich ejecta with higher  $\kappa$ , where  $M_{\text{ej}}$ ,  $v_{\text{ej}}$ , and  $\kappa$  are the mass, velocity, and opacity of the ejecta. Hence heavier ejecta from the merger leads to higher peak magnitude with relatively long duration KNe whereas ejecta with higher velocities have short duration with bright KNe. We see that the lanthanide fraction plays a major role in the light curves, where ejecta with a lower lanthanide fraction decays on a shorter timescale compared to lanthanide-rich ejecta decaying over weeks. From the literature in Nicholl et al. (2021), the study presents an approach where light curves are predicted from the chirp mass, mass ratio, and orbital inclination, including the properties related to the nuclear equation of state. Here we see the nature of light curves based on these physical parameters. It is important to note that Kasen et al. (2017) is based on a radiative transfer model, whereas Nicholl et al. (2021) is based on a semi-analytic model. While KN light curves can be generated with the CVAE, we choose these models due to their different parameterizations and the data availability. However, this does not put any limitations on the use of the CVAE, since data from any other available KN models can be equally used.

## 3. Autoencoder

The advancement of new ML methods and their implicit application in data analysis has opened up a new era in which ML techniques can be implemented to obtain faster results. Time-consuming and resource-draining simulations can be completed on a reasonable timescale (Carleo et al. 2019). There are many available ML techniques that can be used for data analysis with specific techniques built to obtain certain results. We use an autoencoder, an ML technique that is based on a feed-forward mechanism, and its function is to reproduce the input. As is the case with any standard autoencoder, the CVAE consists of three sections, an encoder, a latent space, and a decoder, as shown in Figure 1. The encoder ( $Q(\phi)$ ) compresses the high-dimensional input data into a lower-dimensional latent space while capturing the features of the data. Latent space ( $Z$ ), which is also referred to as the output of the encoder, has a lower-dimensional representation. Generally, a well-trained CVAE has the entire high-dimensional input data smoothly distributed over the latent space. To generate light curves of our choice, we draw samples from this latent space and pass them through the decoder ( $P(\theta)$ ), which takes the compressed representation and generates the required light curves. This facilitates using the CVAE not only as a generative model but also as a tool to quickly look into the parameter dependency of KN light curves. In the CVAE, training is regularized in order to avoid overfitting. Hence, the latent space is well distributed

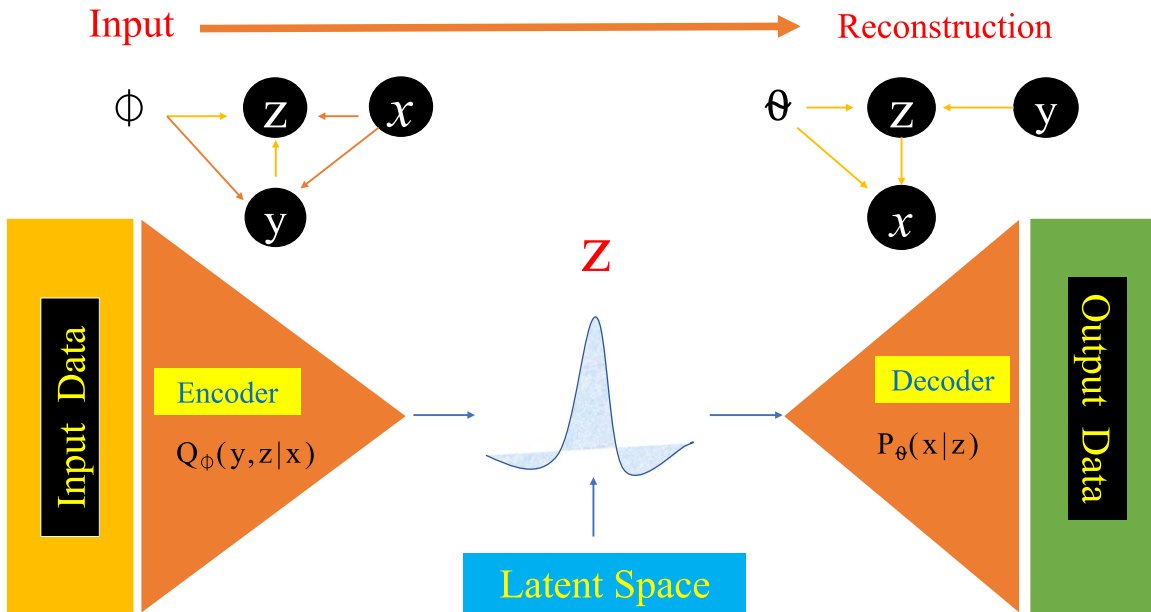


**Figure 1.** Schematic diagram of the CVAE, consisting of an encoder, latent space, and a decoder, from input to data generation. In this figure, we have a probabilistic encoder  $Q(\phi)$  and a probabilistic decoder  $P(\theta)$ .  $Z$  represents the compressed input or encoded representation. Here, the encoder transforms the high-dimensional input data into the low-dimensional latent space, which represents the compressed form of the high-dimensional input data, while the decoder maps this compressed representation in the low-dimensional latent space leading to the reconstruction of the original high-dimensional data. We take a set of data  $x$ , which is the KN light curves, and condition it on a given parameter  $y$ , which is each of the physical parameters from the model, and then the encoder compresses this representation in the latent space. The decoder decompresses the representation and provides the relevant output data, KN light curves, based on the physical parameter values of our choice. This is an overview of the CVAE architecture that is used in this work to train and generate KN light curves.

to enable a generative process. Even though there are other generative models, like generative adversarial networks (GANs) (Goodfellow et al. 2014), since in our work we want to sample new data from the probability distribution of the input data to look at the model parameters crucial for the light curves, we prefer to utilize an autoencoder because of its strong ability to derive a probability distribution of input.

Even though GANs and CVAEs are both generative models and belong to the category of unsupervised learning, one of their primary differences lies in their architecture, where a GAN has a generator and a discriminator and a CVAE has an encoder, latent space, and a decoder. Along with this, the loss functions used in GANs and CVAEs are different from each other. It is important to note that for generating new data, sampling a hidden state in GANs takes place from a predefined distribution, and the sample is then fed into the discriminator, in contrast to that in CVAEs, where sampling of a hidden state, to be fed into the decoder, is done from selecting a prior distribution related to the actual data. Here, to achieve our goal, we take advantage of the CVAE, training it on the light curves by conditioning them on physical parameters and generating new light curves based on physical parameters of our choice. In this case, we have complete control over the generated data set. In this work, we take advantage of this feature of the CVAE to generate new data. In our CVAE architecture, the loss function is a combination of the reconstruction loss and the Kullback–Leibler divergence (Asperti & Trentin 2020). Training is carried out with  $batch\_size = 50$  for  $epochs = 1000$  and with a learning rate of 0.0001. From the training until the generation of light curves for different physical parameter values, it takes  $\simeq 20$  minutes for the process to complete using a 3.9 GHz eight-core Intel Core i9 processor with 32 GB memory. In our training and regeneration of light curves, we do not use the GPU of the system and completely rely on the CPU. Once the

model is trained and saved, it takes only a few milliseconds to generate the light curves. In this section, we outline the CVAE without delving into details; for a more detailed description of variational encoders readers can refer to Kingma & Welling (2013, 2019). In Section 5 more insights into the results obtained from the CVAE are shown.

#### 4. Data

In the ML domain, one needs to be very careful about the data that is fed into the algorithm. The data have to be preprocessed and prepared accordingly. The data used for the training, validation, and test sets are categorized into two types as mentioned in Section 2. We adopt the data from [https://github.com/dnkasen/Kasen\\_Kilonova\\_Models\\_2017](https://github.com/dnkasen/Kasen_Kilonova_Models_2017), hereafter  $D_1$  (Kasen et al. 2017), to prepare the data set to be fed into the CVAE. The physical parameters in this data set are the ejecta mass ( $0.001\text{--}0.1M_{\odot}$ ), the ejecta velocity ( $0.1\text{--}0.3c$ ), and the lanthanide fraction ( $10^{-4}\text{--}10^{-9}$ ). There are 329 light curves with duration of  $\approx 25$  days. Each light curve has different values of the physical parameters within the ranges mentioned above. Light curves are available for different filter bands ( $u$ ,  $g$ ,  $r$ ,  $y$ , and  $z$ ) within the same physical parameter range. Using these data, 241 light curves are used as the training set, and the rest are equally divided into the test set and the validation set. In our analysis, we train the CVAE on each filter band's data separately (hence there are five trained CVAEs) and carry out light-curve generation. However, in the main sections, only the  $g$ -band results are shown; the rest are added in the appendix.

The second type of data used here, hereafter  $D_2$ , consists of simulated light curves at the same filter bands but having different physical parameters. The physical parameters of these data are the chirp mass of the binary system, the mass ratio, the fraction of the remnant disk that is ejected, the viewing angle in degrees from the pole, and the opening angle of the cocoon

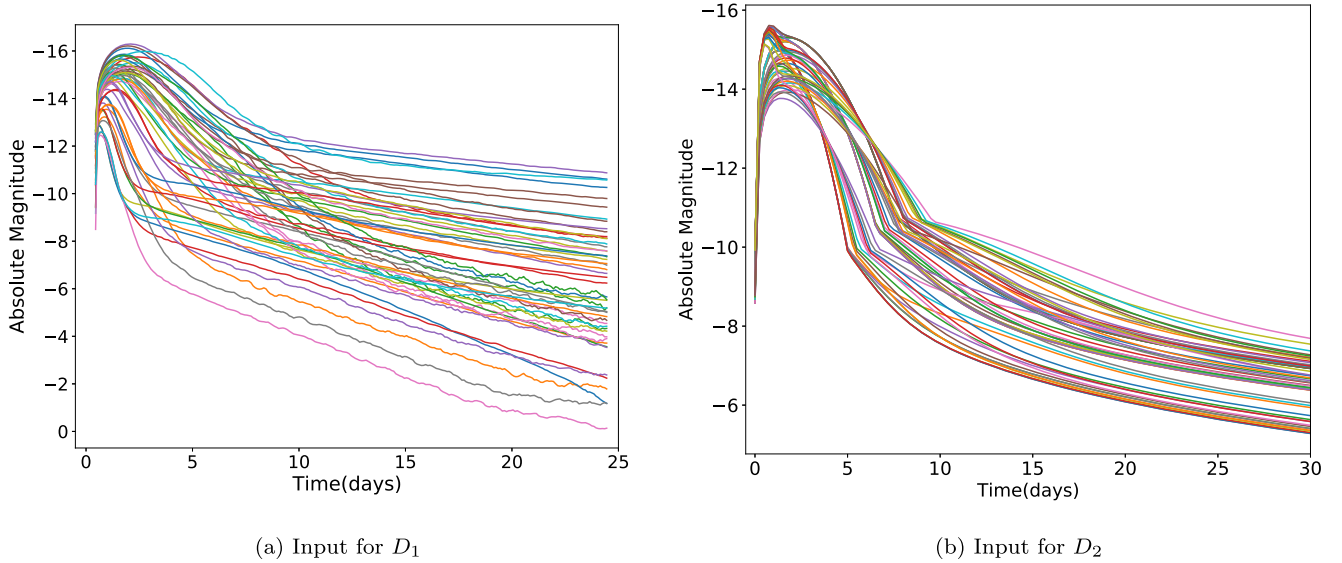


**Figure 2.** (a) In this plot, we present only 50 KN light curves of the  $g$  band of  $D_1$ , which are a part of the data set for training. These light curves consist of the mass of the ejecta, the velocity of the ejecta, and the fraction of lanthanide as physical parameters with values ranging within  $(0.001\text{--}0.1M_\odot)$ ,  $(0.03\text{--}0.05c)$ , and  $(10^{-9}\text{--}10^{-4})$ , respectively. (b) In this plot, we show 50 light curves for the  $g$  band of  $D_2$ , which are a part of the training data set. These light curves consist of the chirp mass, mass ratio, and fraction of the remnant disk with values ranging within  $(0.7\text{--}1.10M_\odot)$ ,  $(0.50\text{--}1.0)$ , and  $(0.15\text{--}0.45)$ , respectively, and a viewing angle of  $0^\circ$  as their physical parameters. This figure gives an outline of the KN light curves and their decay time, which are used for training the CVAE. For both data, the KN light curves are presented in terms of the absolute magnitude. These light curves are scaled within  $[0\text{--}1]$  while being fed into the CVAE for training, but to represent the generated results, these light curves are scaled back to the absolute magnitude.

**Table 1**Physical Parameters of  $D_1$  and  $D_2$  Used for Training and Generating KN Light Curves

Data	Physical Parameters	Data Features
$D_1$	Ejecta Mass ( $M_\odot$ )	0.001, 0.0025, 0.005, 0.01, 0.02, 0.025, 0.03, 0.04, 0.05, 0.075
	Ejecta Velocity ( $c$ )	0.03, 0.05, 0.1, 0.2, 0.3
	Lanthanide Fraction	$10^{-9}$ , $10^{-5}$ , $10^{-4}$ , $10^{-3}$ , $10^{-2}$ , $10^{-1}$
$D_2$	Chirp Mass ( $M_\odot$ )	0.7, 0.8, 0.9, 1.0, 1.1, 1.2, 1.3, 1.4, 1.5, 1.6, 1.7, 1.8
	Mass Ratio	0.5, 0.6, 0.7, 0.8, 0.9, 1.0
	Fraction of the Remnant Disk	0.15, 0.30, 0.45
	Viewing Angle	$0^\circ$ , $60^\circ$ , $90^\circ$

**Notes.**  $D_1$  is taken from [https://github.com/dnkasen/Kasen\\_Kilonova\\_Models\\_2017](https://github.com/dnkasen/Kasen_Kilonova_Models_2017) and  $D_2$  is adopted from <https://github.com/mnicholl/kn-models-nicholl2021>. The training, test, and validation data for the corresponding data set consist of these individual physical parameters.

shock (Nicholl et al. 2021). The ranges of values are  $0.7M_\odot\text{--}2.0M_\odot$  for the chirp mass,  $0.5\text{--}1.0$  for the mass ratio, and  $0.15\text{--}0.45$  for the fraction of the remnant disk. For the viewing angle the data corresponds to values of  $0^\circ$ ,  $60^\circ$ , and  $90^\circ$ . There are 529 light curves having a temporal length of 30 days, out of which 401 are included in the training data and the rest are equally divided into test and validation sets. The difference between the two data sets appears in the physical parameters used in the respective KN models. These data are used to verify the pliability of the CVAE. Since the physical parameters in the two data sets used are entirely different, this gives an extra edge in verifying our approach, and the results

**Table 2**

Interpolated Physical Parameters Used to Simulate Light Curves with MOSFIT for Comparison with the CVAE-generated Light Curves

Data	Physical Parameters	Data Features
$D_2^\dagger$	Chirp Mass ( $M_\odot$ )	1.0, 1.2, 1.4, 1.6, 1.8
	Mass Ratio	0.7, 0.75, 0.8, 0.85, 0.9
	Fraction of the Remnant Disk	0.15, 0.20, 0.25, 0.30, 0.35, 0.40
	Viewing Angle	$45^\circ$ , $60^\circ$ , $75^\circ$ , $90^\circ$

**Note.** Light curves from these physical parameters, alongside those from the test set, are employed to evaluate the performance of the CVAE over the parameter space.

are detailed in Section 5. Since both data sets contain light curves that have different absolute magnitude peak values, while feeding them for training, we scale the light-curve data and the physical parameters between 0 and 1, as this would be a more effective approach. Later, after training and generating light curves, we rescale them and plot them accordingly. Throughout the paper, we follow a particular format to represent the physical parameters in the text and in the legends of the plots. For text and plots relevant to  $D_1$ , we use the format in which  $a$ ,  $b$ , and  $c$  are the values of the ejecta mass in  $M_\odot$ , the velocity of the ejecta in units of the velocity of light, and the lanthanide fraction, respectively. Similarly for  $D_2$ , we use the format of  $[w, x, y, z]$ , where  $w$  is the chirp mass in units of  $M_\odot$ ,  $x$  is the mass ratio,  $y$  gives the fraction of the remnant disk that is ejected, and  $z$  is the viewing angle in degrees from the pole. We use the above format throughout the paper wherever required, without further mentioning the respective units. Figure 2(a) shows 50 of the 329 original light curves from  $D_1$  in the  $g$  band for physical parameters corresponding to ejecta mass, ejecta velocity, and lanthanide fraction with values



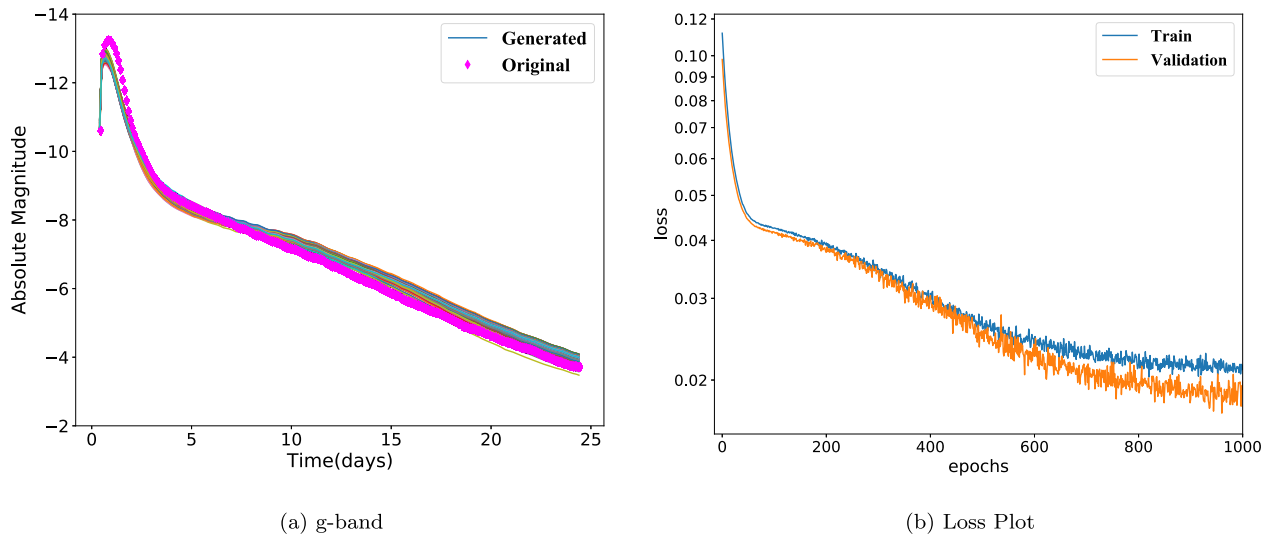


**Figure 3.** (a) This figure shows the light curves' comparison corresponding to the  $g$  band after training and generation are implemented on  $D_1$ . We display 100 light curves for the physical parameters of ejecta mass, ejecta velocity, and lanthanide fraction having values of  $[0.001M_{\odot}, 0.03c, \text{ and } 10^{-5}]$  alongside the light curve from the test data for the same physical parameters. The original light curve is shown in diamond markers and is within the distribution of the generated light curves shown by solid lines. The deviations seen in the generated light curves arise from the variations in the latent space. (b) This plot corresponds to the learning curve after we implement the CVAE. The gap between the two curves is small indicating a good fit.

ranging within  $0.001\text{--}0.1M_{\odot}$ ,  $0.03\text{--}0.05c$ , and  $10^{-4}\text{--}10^{-9}$ , respectively, whereas in Figure 2(b), we show 50 of the 529 light curves corresponding to  $D_2$  having the physical parameters of chirp mass ( $0.7\text{--}1.10M_{\odot}$ ), mass ratio ( $0.5\text{--}1.0$ ), fraction of the remnant disk ( $0.15\text{--}0.45$ ), and viewing angle of  $0^{\circ}$  from the pole as mentioned in Section 4. In Figure 2, we show the input light curves corresponding to  $D_1$  and  $D_2$  that are fed into the CVAE. During training and validation, scaled values of the KN light curves and the conditional physical parameters are used for both  $D_1$  and  $D_2$ , and the obtained results are shown in absolute magnitude values. The input for training from  $D_1$  consists of 241 light curves and that from  $D_2$  has 401 light curves from the  $g$  band. As previously mentioned, each light curve has different physical parameters corresponding to the ejecta mass, ejecta velocity, and lanthanide fraction for  $D_1$  and to the chirp mass, mass ratio, fraction of the remnant disk, and viewing angle from the pole for  $D_2$ . Throughout the text,  $D_1$  and  $D_2$  are referred to accordingly, keeping the above training, test, and validation sets unchanged. In Table 1, we tabulate the physical parameters and the data ranges used in this work. In this study, while defining the training, test, and validation sets we do not restrict the physical parameters to different regions of the parameter space. Instead, the physical parameters present in the training, test, and validation sets cover the entire parameter space. At the same time, we ensure that none of the parameter combinations, i.e., ejecta mass, ejecta velocity, and lanthanide fraction for  $D_1$  and chirp mass, mass ratio, fraction of the remnant disk, and viewing angle for  $D_2$ , are repeated in the training, test, and validation sets. Specifically, for  $D_2$ , apart from the training, test, and validation sets, we put aside a separate set of simulated light curves from MOSFiT,<sup>6</sup> which are utilized to evaluate the performance of the CVAE. We augment the existing test set with these separately simulated light curves, hereafter  $D_2^{\dagger}$ , to provide a robust performance check. The combination of

physical parameters present in  $D_2^{\dagger}$ , as shown in Table 2, covers the parameter space but is previously unseen to the CVAE. The CVAE will be employed with these sets of physical parameters to generate light curves to be compared with the true light curves, thus providing a robust approach to appraising the CVAE's performance. Hence, using the CVAE, we generate light curves over a grid on the parameter space.

## 5. Results

In this section, we present the results after the implementation of the CVAE. After training, samples are drawn from the latent space to reconstruct light curves based on the required physical parameters. This section points out the comparison between the generated light curves from the latent space and the original light curves from the simulation. This technique allows us to generate as many light curves as we require over a wide range of physical parameters within the range provided by the model.

In Figure 3(a), we show the generated light curves of the  $g$  band after implementing the CVAE for the physical parameters of  $[0.001M_{\odot}, 0.03c, \text{ and } 10^{-5}]$ , which are the ejecta mass, ejecta velocity, and lanthanide fraction, respectively, as mentioned in Section 4. The loss plot for the CVAE is shown in Figure 3(b). We find that the validation loss and the training loss decrease to a point of stability and there is a small gap between the two curves. Although the CVAE has the ability to generate as many light curves as we want for one or many physical parameters, in order to avoid congestion in the plots, we limit ourselves to 100 generated light curves based on the above physical parameters. The 100 light curves are closely spaced and the apparent variations at later days come from the variations of the probability distribution in the latent space. These variations are expected since, to regenerate light curves, we randomly draw samples from the latent space. This randomness allows the CVAE to produce variations in the light curves even for the same input. Thus, we see these variations in the CVAE-generated light curves for the physical

<sup>6</sup> <https://github.com/guillochon/MOSFiT>

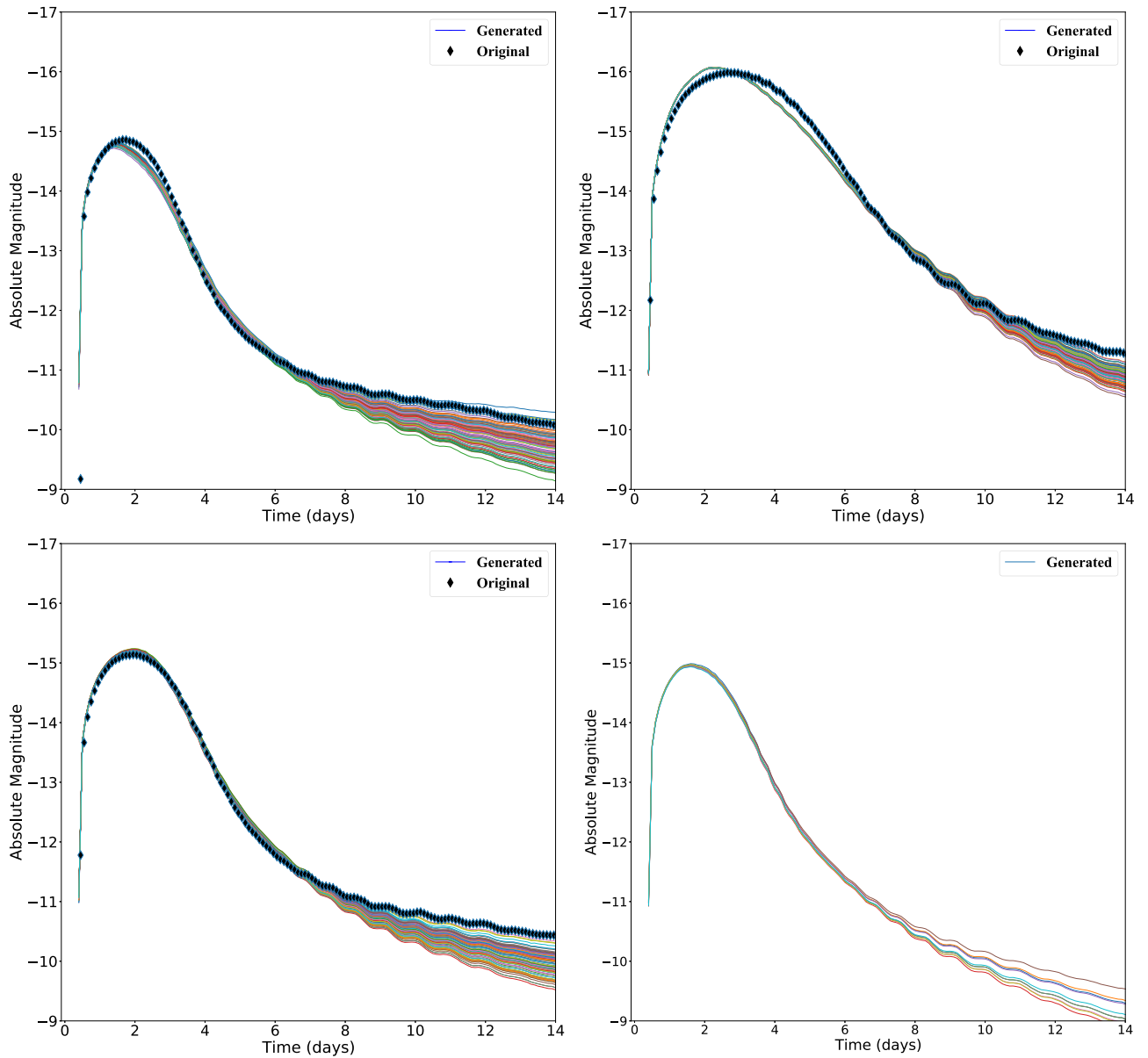


**Figure 4.** In this figure, we compare 100 light curves (solid lines) generated from the CVAE with the original light curves (diamond markers) for ejecta masses of  $0.02M_{\odot}$  (upper left),  $0.1M_{\odot}$  (upper right), and  $0.03M_{\odot}$  (bottom left) keeping the ejecta velocity ( $0.03c$ ) and lanthanide fraction ( $10^{-9}$ ) constant for all the generated light curves. These values of the physical parameters are chosen from the test set. In the bottom right panel, 10 light curves for an arbitrary physical parameter configuration [ $0.025M_{\odot}$ ,  $0.035c$ , and  $10^{-5}$ ] are shown. All the generated and original light curves correspond to the  $g$  band.

parameters. Besides, the light curves are more sensitive to changes in the physical parameters in later days. However, since we are more interested in the earlier KN evolution, we restrict the plots to 14 days. This parameter is chosen from the simulated data in order to verify the robustness of the CVAE. It is clear that the input light curve (shown by diamond markers) used from the validation data of the CVAE is well within the limit of the regenerated light curves.

This confirms that the CVAE is well trained. In Figure 3(a), we see some overlapping in the light curves, since the 100 generated light curves have relatively similar values. While generating these light curves, samples are drawn from different points in the latent space. It is possible to generate as many light curves as desired and observe the possible variations from the latent representation. Since the encoder maps the input light curves to a probability distribution over the latent space, even

though in the respective KN models there is only one light curve associated with a single value of the physical parameter, implementing the CVAE provides a comparatively wide range of the light-curve distribution for the same value of the physical parameter arising from the latent representation. This variation of the generated KN light curves is particularly interesting when the light curves are generated for an entirely new physical parameter set that the CVAE has not come across during training and validation.

KN light curves are extremely sensitive to the ejecta mass (Kasen et al. 2017). With a change in the ejecta mass, the peak value of the light curves increases and shifts to later days, which is explicitly shown in the top left, top right, and bottom left panels in Figure 4. This result is expected in accordance with the KN evolution. In this figure, a comparative analysis for different values of the ejecta mass ( $0.02M_{\odot}$ ,  $0.1M_{\odot}$ , and

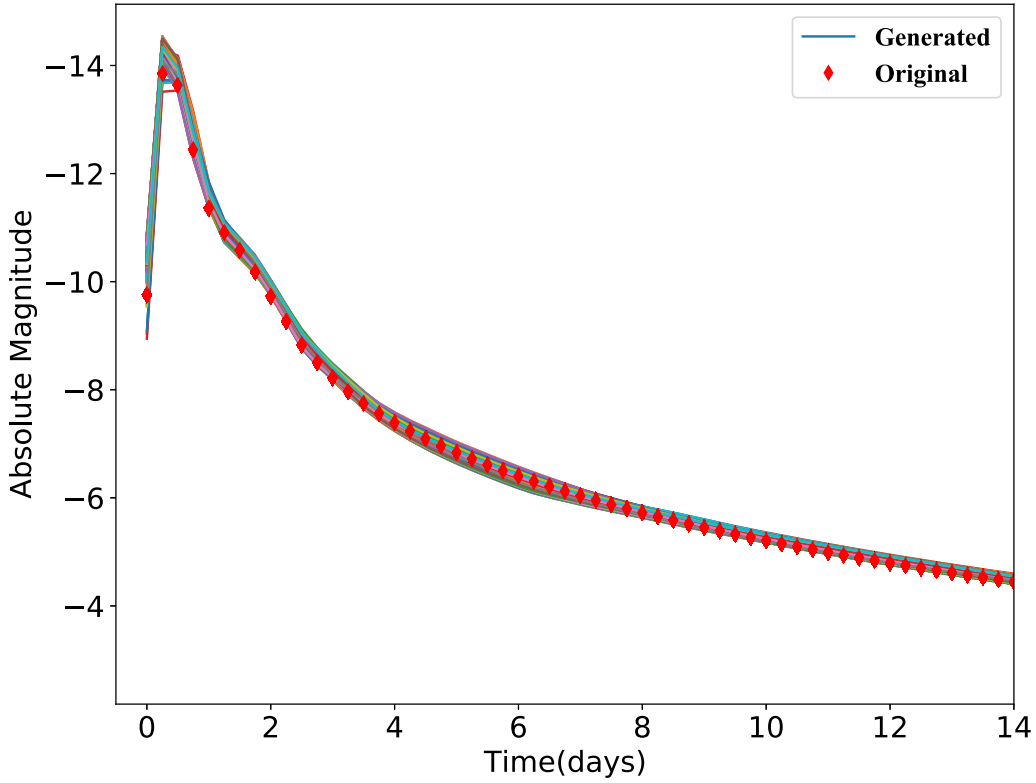


**Figure 5.** Comparison for the true and generated light curves corresponding to  $D_2$ . These 100 light curves from the  $r$  band are generated from the CVAE, for which comparison is shown with the physical parameters of chirp mass, mass ratio, fraction of the remnant disk, and viewing angle from the pole having values of  $[1.8M_\odot, 0.9, 0.15, \text{ and } 90^\circ]$ , respectively. The diamond markers correspond to the true light curve, whereas the solid lines correspond to the CVAE-generated light curves. The physical parameter for the true light curve is taken from the test set for verifying with the generated ones.

$0.03M_\odot$ ) is shown keeping the ejecta velocity ( $0.03c$ ) and lanthanide fraction ( $10^{-9}$ ) unchanged. One hundred light curves are generated from the CVAE compared with the original light curve for the above physical parameters. In the bottom right panel, the light curve for an arbitrary parameter configuration ( $0.025M_\odot$ ,  $0.035c$ , and  $10^{-5}$ ) is shown. This physical parameter value configuration is not present in  $D_1$ ; therefore we do not have any benchmark to validate it with. However, with more data from the respective KN model, this can be verified. Similar comparative analysis, for all other filter bands, showing the evolution of the light curves with changes in ejecta masses, ejecta velocities, and lanthanide fractions is shown in the appendix in Figure A1. We next take the second data set,  $D_2$ , with physical parameters of chirp mass, mass ratio, fraction of the remnant disk, and viewing angle from the pole. We run the same analysis as above. As mentioned in Section 4, this data set has a total of 529 light curves, with the above physical parameters having the values given in that section. The training data has 401 light curves, and the remaining are equally divided into a test set and a validation set. In Figure 5, we demonstrate the application of the CVAE on  $D_2$ , where we compare 100 light curves generated from the CVAE with the original light curve for the physical parameters of  $[1.8M_\odot, 0.9, 0.15, \text{ and } 90^\circ]$  correlated to the chirp mass, the mass ratio, the fraction of the remnant disk, and the viewing angle from the pole, respectively. This set of physical parameters is taken from the test data set.

The input light curve is within the distribution of the generated light curve, which indicates that the CVAE is performing well and the training and regeneration of the light curves are successful. Figure 6 shows the confidence plot for a

set of physical parameters where it is important to mention that the neural network has not seen this set of physical parameters and hence from the similarity between the generated and true light curves we can substantiate the performance of the CVAE. Other relevant plots for different combinations of physical parameters and changes in the light curves corresponding to other filter bands are shown in Figure B1 in the appendix. To measure the predictive accuracy of the trained CVAE, we use the mean absolute error (MAE), where a lower value corresponds to a more accurate prediction, calculated using

$$\text{MAE} = \frac{1}{n} \sum_{i=1}^n |y_i - \hat{y}_i|, \quad (1)$$

where  $y_i$  and  $\hat{y}_i$  are the true values and predicted values of the light curves of the test data and  $n$  is the total number of points drawn for each light curve from latent space. Alongside the above MAE, we calculate and plot the mean squared error (MSE) between the true and predicted light-curve values using the equation

$$\text{MSE} = \frac{1}{n} \sum_{i=1}^n (z_i - \hat{z}_i)^2 \quad (2)$$

where  $n$  is the total number of data points and  $z_i$  and  $\hat{z}_i$  are the respective values of the true and CVAE-predicted light curves.

## 6. Discussion

Since the CVAE depends on the input data, light curves from different KN models can be used for training and the corresponding trained CVAE is saved for generating light

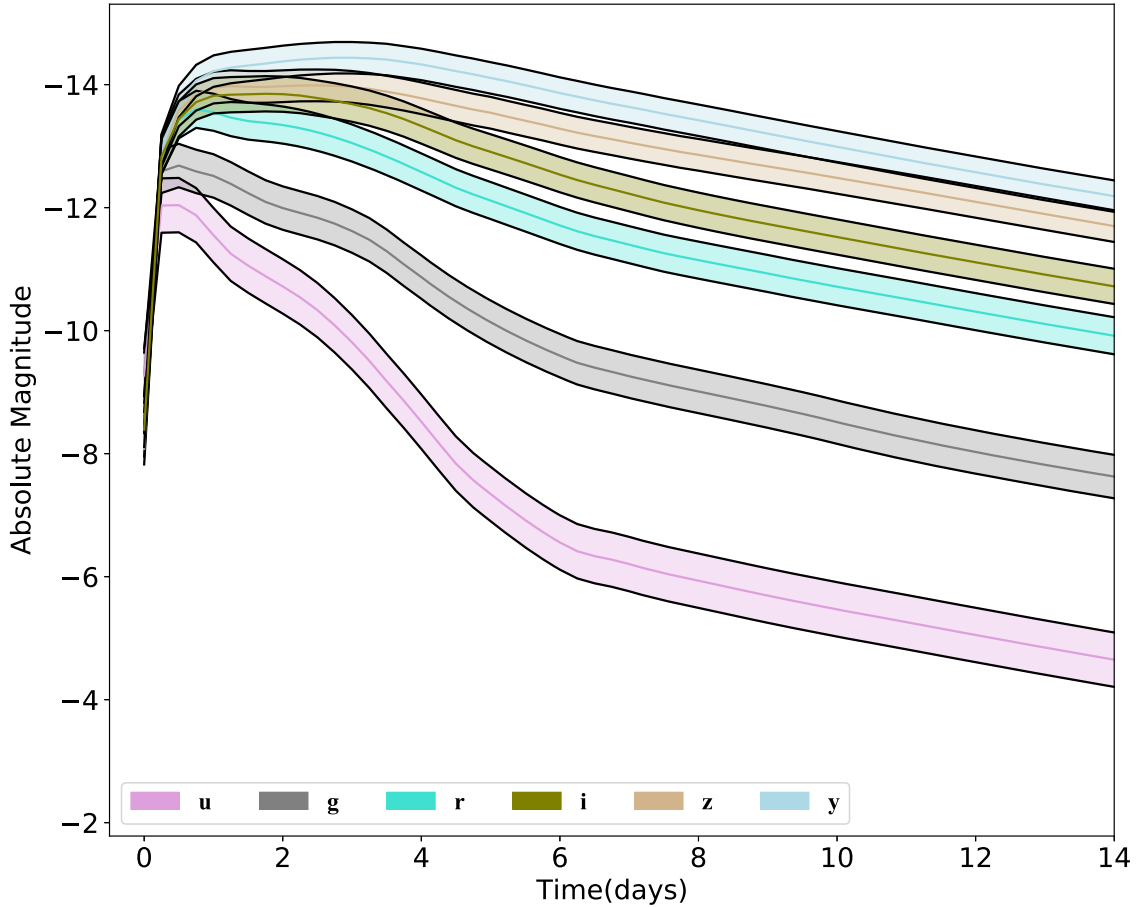


**Figure 6.** This figure corresponds to the 90% confidence plot for the CVAE-generated and true light curves in the  $g$ ,  $r$ ,  $z$ ,  $y$ ,  $i$ , and  $u$  bands that have the physical parameters of  $1.2M_{\odot}$  chirp mass, 0.7 mass ratio, 0.15 fraction of the remnant disk, and a viewing angle of  $60^{\circ}$ . True values of the light curves for the above parameters are represented by the solid lines in each color-filled region. We find quite satisfactory agreement between the true and CVAE-generated light curves. The light curves corresponding to the above parameters are taken from the  $D_2^{\dagger}$  data set and thus are entirely new to the CVAE for prediction and generation.

curves. The input data contains both training data and physical parameters. This versatility of the technique provides a unique opportunity to test this on other data sets. Using Equation (1), we have MAEs of 0.0995 and 0.0339 for  $D_1$  and  $D_2$ , respectively. The MSEs for  $D_1$  and  $D_2$  calculated on the test data using Equation (2) are 0.00241 and 0.00153, respectively.

Compared to that for  $D_2$ , the MAE for  $D_1$  is higher, as the number of training data is relatively lower for  $D_1$ . We not only successfully reconstruct the light curves for known values of the physical parameters but also generate light curves for physical parameters that are not present in the data set but are well within the range of the physical parameter values provided in the respective models. In Figure 3, we present the reconstructed light curves and the corresponding loss values for the CVAE. Based on these results, we proceed to generate light curves for different combinations of physical parameters and verify those as presented in Figure 4. The obtained results are consistent with the KN evolution presented in the model. Comparing the plots in Figures 3(a) and 4, as mentioned in Section 5, we can see more variations in the latter, and for the latter figure the light curves are truncated to 14 days while in the former, the CVAE-generated light curves are extended until the end. For the plots generated from  $D_2$ , since there is no significant change of astrophysical importance, we truncate the light curves to 14 days. Model evaluation is performed with the test data, and in the current work, we move a step ahead to evaluate performance via the confidence interval (Figure 6) and

MSE (Figure 7) between the CVAE-generated and true light curves by taking physical parameters from  $D_2^{\dagger}$ , which contains the physical parameters from the test set as well as entirely new physical parameters that are absent in the training, test, and validation sets. Therefore, as mentioned in Section 4, we use the physical parameter combination from Table 2 to produce Figure 7. Therefore, when evaluating performance on these sets of previously unseen parameters, we simulate the real scenario akin to observing a new KN. In Figure 6, we present the 90% confidence interval between the generated and true light curves in different filter bands of  $u$ ,  $g$ ,  $r$ ,  $i$ ,  $z$ , and  $y$  having a chirp mass of  $1.2M_{\odot}$ , a mass ratio of 0.7, a 0.15 fraction of the remnant disk, and a viewing angle of  $60^{\circ}$ . The true light curves for this set of parameters are not included in the training, test, or validation data set; thus this data is unseen to the network. To plot the confidence interval, we take the mean light curves from the 2000 CVAE-generated light curves for the above physical parameter values [ $1.2M_{\odot}$ , 0.7, 0.15,  $60^{\circ}$ ] in each filter band. Each result is highlighted with a color-shaded region for each filter band including the true light curve. Here we see good agreement between the true and generated light curves, which provides supporting evidence in favor of the performance of the CVAE. In addition to the above, we calculate the MSE between the generated and true light curves, where we obtain an error that is always within (0.015–0.08) for the above set of physical parameters. To provide further evidence of the CVAE's performance, we illustrate the MSE calculated over the entire



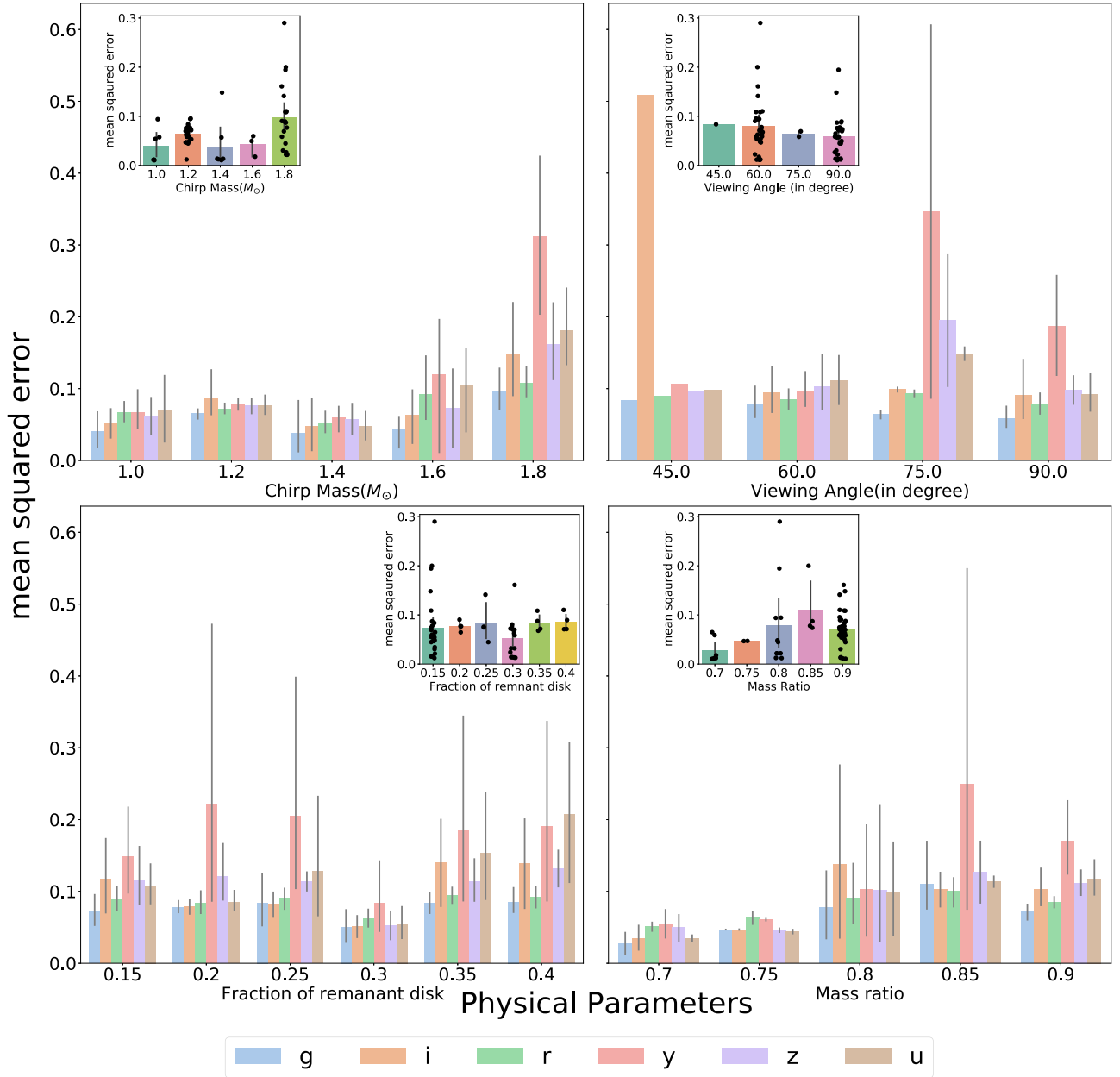


**Figure 7.** In this figure, we present the performance of the CVAE spanning the whole parameter space of chirp mass ( $1.0M_{\odot}$ – $1.80M_{\odot}$ ), viewing angle ( $45^{\circ}$ – $90^{\circ}$ ), fraction of the remnant disk ( $0.15$ – $0.40$ ), and mass ratio ( $0.70$ – $0.90$ ) in the  $u$ ,  $g$ ,  $i$ ,  $r$ ,  $z$ , and  $y$  filter bands represented by the different color bars grouped accordingly. The  $y$ -axis represents the mean squared values whereas in the  $x$ -axis we have the respective physical parameter values for which we have calculated the overall MSE in the different filter bands shown with different color bars. For the chirp mass frame (upper left), the MSEs for the different filter bands are grouped by the chirp mass values,  $1.0M_{\odot}$ ,  $1.2M_{\odot}$ ,  $1.4M_{\odot}$ ,  $1.6M_{\odot}$ , and  $1.8M_{\odot}$ , while covering the parameter space of viewing angle, mass ratio, and fraction of the remnant disk. For the viewing angle frame (upper right), we show the error for  $45^{\circ}$ ,  $60^{\circ}$ ,  $75^{\circ}$ , and  $90^{\circ}$  viewing angles calculated over the entire parameter values of chirp mass, mass ratio, and fraction of the remnant disk. In the remnant disk frame (lower left), for values of  $0.15$ ,  $0.20$ ,  $0.25$ ,  $0.30$ ,  $0.35$ , and  $0.40$  of the fraction of the remnant disk, errors are grouped in the different filter bands encompassing the chirp mass, viewing angle, and mass ratio. For the mass ratio frame (lower right), errors corresponding to mass ratio values of  $0.70$ ,  $0.75$ ,  $0.80$ ,  $0.85$ , and  $0.90$  are shown as grouped bar plots across the parameter space of chirp mass, viewing angle, and fraction of the remnant disk for the different filter bands. In the insets for all the frames, we show the CVAE's performance over the entire parameter space, as discussed above, obtained from the CVAE-generated  $g$ -band light curves. Each dot in the inset corresponds to the calculated value of the MSE of a light curve for the relevant set of physical parameters. For each of the histograms corresponding to a different parameter space, error bars are shown. The histograms without error bars correspond to a single light curve that is available for calculating the MSE between the true and CVAE-generated light curves.

parameter space while considering the following values of physical parameters for the different filter bands:  $1.0M_{\odot}$ ,  $1.2M_{\odot}$ ,  $1.4M_{\odot}$ ,  $1.6M_{\odot}$ , and  $1.8M_{\odot}$  for the chirp mass region;  $45^{\circ}$ ,  $60^{\circ}$ ,  $75^{\circ}$ , and  $90^{\circ}$  for the viewing angle region;  $0.15$ ,  $0.20$ ,  $0.25$ ,  $0.30$ ,  $0.35$ , and  $0.40$  for the fraction of the remnant disk parameter; and  $0.70$ ,  $0.75$ ,  $0.80$ ,  $0.85$ , and  $0.90$  for the mass ratio parameter (as shown in Figure 7). To calculate the MSE,

we use the mean of 2000 CVAE-generated light curves and the true light curves for the respective sets of physical parameters.

Figure 7 consists of four frames, each having an inset, which show the error calculated for the respective value of the physical parameter (along the  $x$ -axis) across the parameter space of the other physical parameters. For the chirp mass frame (upper left), the error is calculated for different chirp

masses ( $1.0M_{\odot}$ ,  $1.2M_{\odot}$ ,  $1.4M_{\odot}$ ,  $1.6M_{\odot}$ , and  $1.8M_{\odot}$ ) across the parameter space of the viewing angle, the mass ratio, and the fraction of the remnant disk, grouped together for each value of the chirp mass for the different filter bands. For the viewing angle frame (upper right), for values of  $45^{\circ}$ ,  $60^{\circ}$ ,  $75^{\circ}$ , and  $90^{\circ}$  the error is calculated across the chirp mass, mass ratio, and fraction of the remnant disk and grouped accordingly. For calculating the MSE for the fraction of the remnant disk, we consider 0.15, 0.20, 0.25, 0.30, 0.35, and 0.40 across the parameter space of chirp mass, viewing angle, and mass ratio grouped by the parameter values in the different filter bands. In the mass ratio frame (lower right), the error is calculated for mass ratio values of 0.70, 0.75, 0.80, 0.85, and 0.90, across the parameter space of chirp mass, viewing angle, and fraction of the remnant disk grouped accordingly. Certain sets of physical parameters in certain filter bands tend to have comparatively high MSE values, adding more to the overall error. For instance, the above case can be seen in the viewing angle frame in Figure 7 for the  $45^{\circ}$  viewing angle in the  $i$  band. However, the overall error is considerably low. In the insets of Figure 7, the  $g$ -band results are shown, where each dot refers to the MSE of a single light curve for the respective set of physical parameters across the parameter space. Here also, we find that for certain sets of physical parameters, the error value is higher as evident from outliers in the  $1.8M_{\odot}$  chirp mass,  $60^{\circ}$  viewing angle, 0.15 fraction of the remnant disk, and 0.80 mass ratio in the insets. In comparison to one–one MSEs, the overall error is higher as it includes all the parameter sets across the individual parameter considered. From the above result, we find the regions in parameter space for the different filter bands where the CVAE has comparatively unsatisfactory results. While comparing Figures 3 and 4 for  $D_1$  with the results from  $D_2$  in Figure 5, one will find similar deviations in the tail of the light curves after 10 days for the different sets of physical parameters shown in the plots presented in the appendix (Figure A1 and B1). In the main text, only one such plot (Figure 5) is shown for a single set of physical parameters, where the deviations are smaller. One of the main reasons for such different deviations is the distribution of the latent space owing to the difference in the number of training data, since  $D_1$  has less training data than  $D_2$ . In addition to the above, a summary of the network (Figure C1) is presented in the appendix for reference.)

## 7. Conclusion

In this paper, we look into rapid generation of KN light curves based on different physical parameter values while implementing a CVAE. We present a methodological approach to our idea. In the initial stages, a performance check is carried out while inspecting the loss curves during the training and validation. We also evaluate the CVAE's performance on different physical parameters from the test data, and hence perform rapid interpolation of light curves and subsequently provide evidence that the results are quite in agreement with the true light curves. However, in certain cases, we find that for  $D_1$ , as compared to the original light curves, the generated light curves tend to deviate after 8 days but for  $D_2$  we do not see such deviations in later days. Here, we use publicly available KN data to provide a proof of concept, but this does not put any

limitation on our technique. This technique can also be used for similar kinds of data analysis comprising data related to other domains in astronomy and astrophysics. The striking point for such an approach is that it reduces the time that is required by simulations to rerun and reproduce similar results for different physical parameters every time. We train the data that are available and produce the desired results rapidly rather than adjust the simulation code each time and the saved CVAE model can be used to generate the required KN light curves. In this work, by speeding up the light-curve generation by 1000 times, we have achieved rapid results. Besides the current application for KNe, the CVAE technique demonstrated above has prospective applications in a similar procedure where data are available for training, test, and validation. In the current work, since the detailed calculations of the simulation are not incorporated into the CVAE, we do not expect any new results, but at the same time, the trained CVAE produces results without looking into the particulars of the simulation. An alternative approach for generating simulation results, with the help of ML tools, without actually re-executing the simulation is presented here. Additionally, this method can accommodate other KN models where data are available to be fed into the network. This kind of CVAE approach also has potential to be utilized for rapid parameter estimation not only for KNe but also for other astrophysical sources for which rapid data analysis is required.

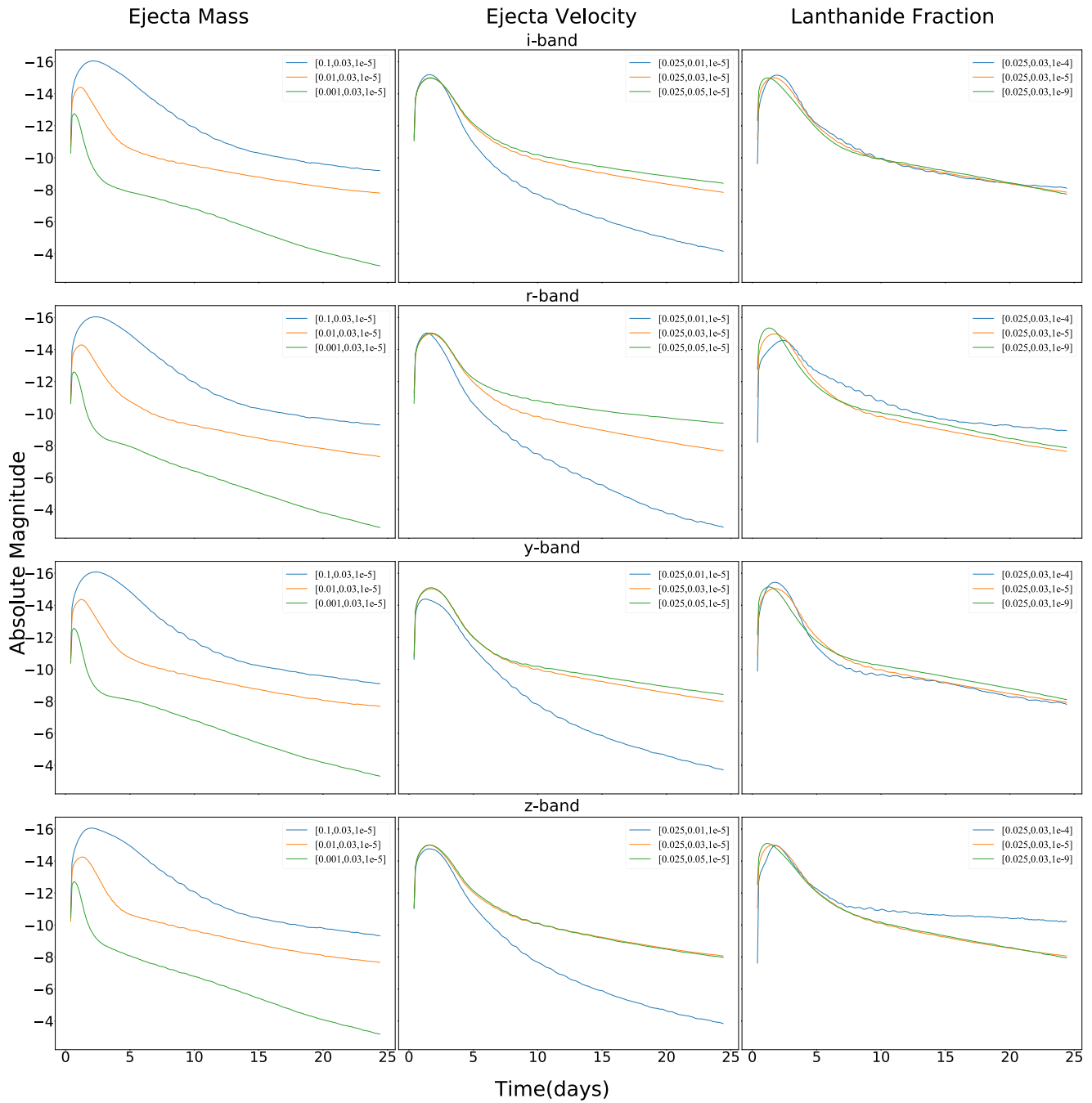
## Acknowledgments

This work is supported by the National Science and Technology Council of Taiwan under the grants 110-2628-M-007-005 and 111-2112-M-007-020, and by a joint grant of the National Science and Technology Council and the Royal Society of Edinburgh through 110-2927-I-007-513. M.J.W. is supported by the Science and Technology Facilities Council [2285031,ST/V005634/1,ST/V005715/1]. I.K.S.H. is supported by the Science and Technology Research Council [ST/L000946/1]. I.K.S.H. and M.J.W. are also supported by the European Cooperation in Science and Technology (COST) action [CA17137]. M.N. is supported by the European Research Council under the European Union's Horizon 2020 research and innovation program (grant agreement No. 948381) and by funding from the UK Space Agency. The authors are grateful for the valuable suggestions from He-Feng Hsieh, John Veitch, and Nicola De Lillo.

*Software:* matplotlib (Hunter 2007), pandas (The pandas development team 2020), tensorflow (Abadi et al. 2015), keras (Chollet et al. 2015), MOSFiT (<https://github.com/mnicholl/MOSFiT>, <https://github.com/guillochon/MOSFiT>).

## Appendix A Additional Results of Other Filter Bands after Implementing CVAE on $D_1$

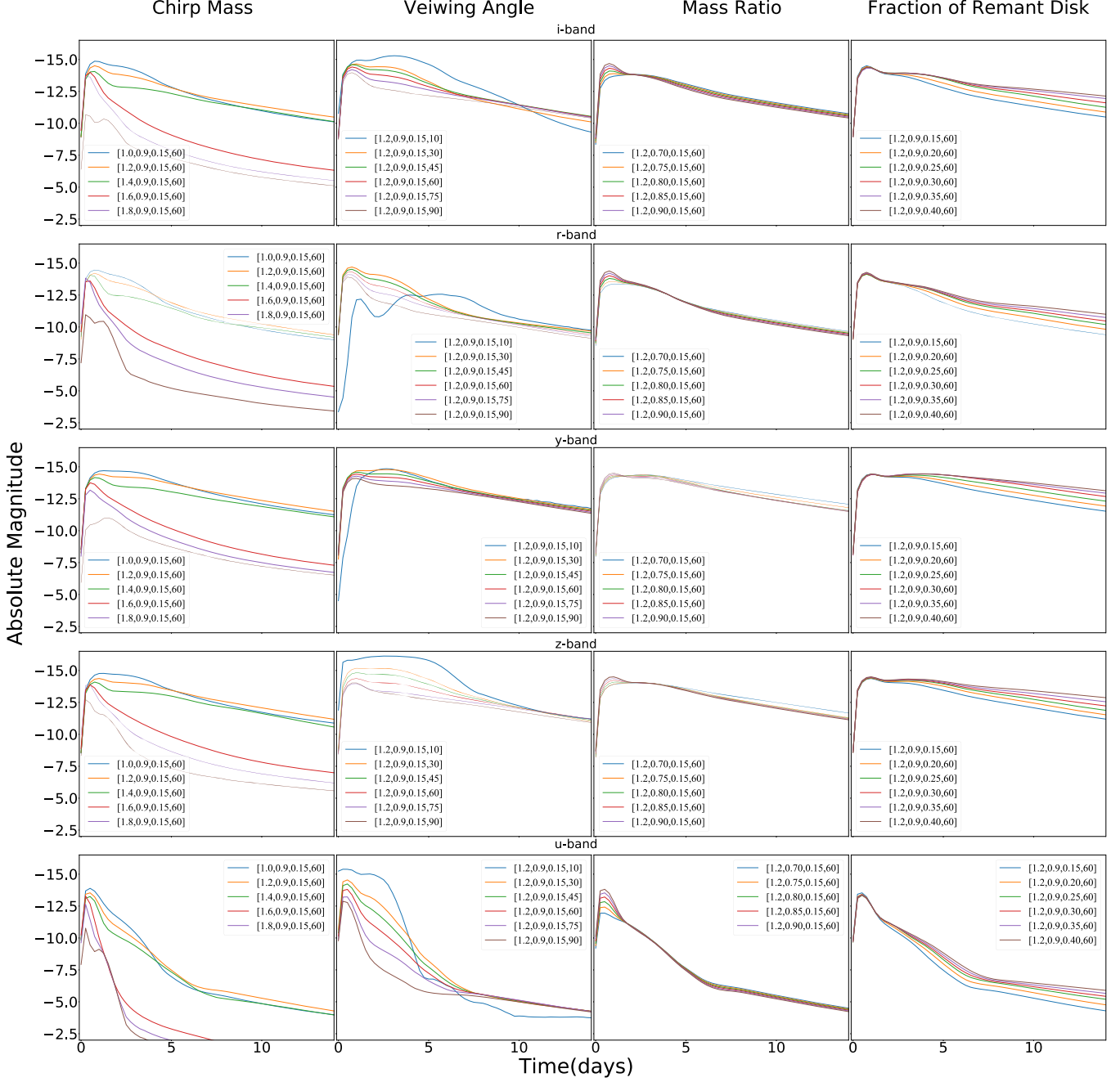
Figure A1 shows the comparative analysis of the light curves for  $D_1$  with changes in ejecta masses, ejecta velocities, and lanthanide fractions for the different filter bands.



**Figure A1.** This figure encompasses the CVAE-generated light curves for different values of physical parameters for the respective filter bands. In each row of the figure, the light curves correspond to different ejecta masses having values of ( $0.1M_{\odot}$ ,  $0.01M_{\odot}$ ,  $0.001M_{\odot}$ ) with the ejecta velocity ( $0.03c$ ) and lanthanide fraction ( $10^{-5}$ ) kept constant, to different ejecta velocities having values of ( $0.01c$ ,  $0.03c$ ,  $0.05c$ ) with the ejecta mass ( $0.025M_{\odot}$ ) and lanthanide fraction ( $10^{-5}$ ) kept constant, and to different lanthanide fractions having values of ( $10^{-4}$ ,  $10^{-5}$ ,  $10^{-9}$ ) with the ejecta mass ( $0.025M_{\odot}$ ) and ejecta velocity ( $0.03c$ ) kept constant for the *i*, *r*, *y*, or *z* filter band.

### Appendix B Additional Results of Other Filter Bands after Implementing CVAE on $D_2$

Figure B1 shows the evolution of the light curves for  $D_2$  with changes in chirp mass, viewing angle, mass ratio, and the fraction of the remnant disk for different filter bands.

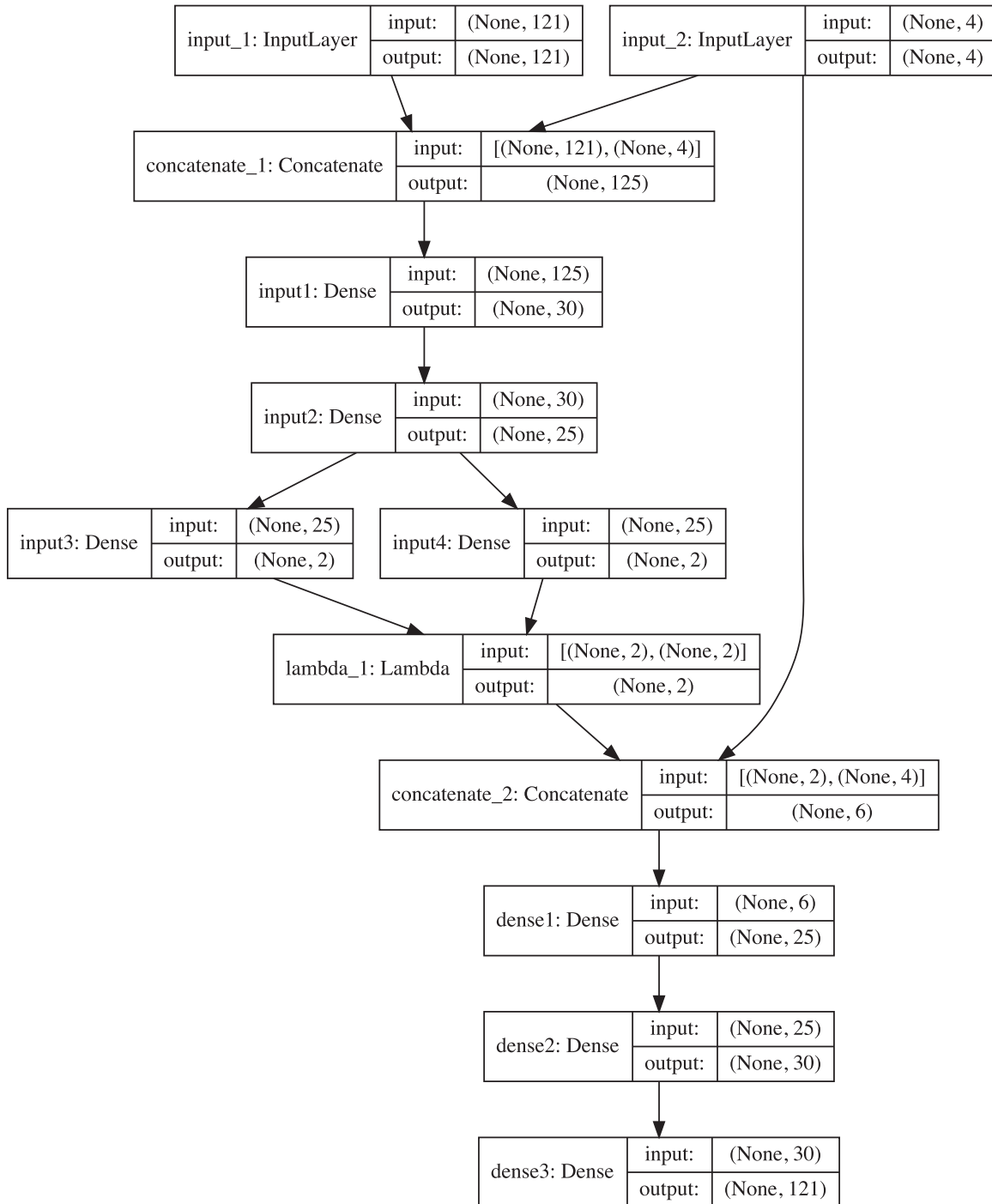


**Figure B1.** This figure demonstrates the evolution of light curves for the different physical parameters of chirp mass, viewing angle, mass ratio, and fraction of the remnant disk. In each row of the plot, we bring together the CVAE-generated light curves for different chirp mass values ( $1.0M_{\odot}$ ,  $1.2M_{\odot}$ ,  $1.4M_{\odot}$ ,  $1.6M_{\odot}$ ,  $1.8M_{\odot}$ ) while keeping the viewing angle ( $60^{\circ}$ ), mass ratio (0.9), and fraction of the remnant disk (0.15) constant; those for different viewing angles having values of ( $10^{\circ}$ ,  $30^{\circ}$ ,  $45^{\circ}$ ,  $60^{\circ}$ ,  $75^{\circ}$ ,  $90^{\circ}$ ) from the pole while keeping the chirp mass ( $1.2M_{\odot}$ ), mass ratio (0.9), and fraction of the remnant disk (0.15) constant; those for different mass ratios of (0.70, 0.75, 0.80, 0.85, 0.90) while keeping the chirp mass ( $1.2M_{\odot}$ ), fraction of the remnant disk (0.15), and viewing angle ( $60^{\circ}$ ) constant; and those for different fractions of the remnant disk having values of (0.15, 0.20, 0.25, 0.30, 0.35, 0.40) while keeping the chirp mass ( $1.2M_{\odot}$ ), mass ratio (0.9), and viewing angle ( $60^{\circ}$ ) constant for the  $i$ ,  $r$ ,  $y$ ,  $z$ , or  $u$  filter band.






**Appendix C**  
**Summary of the CVAE**

Figure C1 shows a summary of the CVAE network.



**Figure C1.** This is a summary of the CVAE implemented in the current work.

**ORCID iDs**

Surojit Saha  <https://orcid.org/0000-0002-3333-8070>  
 Michael J. Williams  <https://orcid.org/0000-0003-2198-2974>  
 Laurence Datrier  <https://orcid.org/0000-0002-0290-3129>  
 Fergus Hayes  <https://orcid.org/0000-0001-7628-3826>

Matt Nicholl  <https://orcid.org/0000-0002-2555-3192>  
 Albert K. H. Kong  <https://orcid.org/0000-0002-5105-344X>  
 Martin Hendry  <https://orcid.org/0000-0001-8322-5405>  
 IK Siong Heng  <https://orcid.org/0000-0002-1977-0019>  
 Gavin P. Lamb  <https://orcid.org/0000-0001-5169-4143>  
 En-Tzu Lin  <https://orcid.org/0000-0002-0030-8051>  
 Daniel Williams  <https://orcid.org/0000-0003-3772-198X>

## References

- Abadi, M., Agarwal, A., Barham, P., et al. 2015, TensorFlow: Large-scale Machine Learning on Heterogeneous Systems, <https://www.tensorflow.org/>
- Abbott, B. P., Abbott, R., Abbott, T. D., et al. 2017a, *ApJL*, **848**, L12
- Abbott, B. P., Abbott, R., Abbott, T. D., et al. 2017b, *PhRvL*, **119**, 161101
- Arcavi, I., McCully, C., Hosseinzadeh, G., et al. 2017, *ApJL*, **848**, L33
- Asperti, A., & Trentin, M. 2020, *IEEFA*, **8**, 199440
- Ball, N. M. 2011, arXiv:1110.5688
- Ball, N. M., & Brunner, R. J. 2010, *IJMPD*, **19**, 1049
- Barnes, J., & Kasen, D. 2013, *ApJ*, **775**, 18
- Carleo, G., Cirac, I., Cranmer, K., et al. 2019, *RvMP*, **91**, 045002
- Chollet, F., et al. 2015, Keras, <https://github.com/fchollet/keras>
- Coulter, D. A., Foley, R. J., Kilpatrick, C. D., et al. 2017, *Sci*, **358**, 1556
- Coward, D. M., Branchesi, M., Howell, E. J., Lasky, P. D., & Böer, M. 2014, *MNRAS*, **445**, 3575
- Cowperthwaite, P. S., Berger, E., Villar, V. A., et al. 2017, *ApJL*, **848**, L17
- Eichler, D., Livio, M., Piran, T., & Schramm, D. N. 1989, *Natur*, **340**, 126
- Fong, W., Berger, E., Margutti, R., & Zauderer, B. A. 2015, *ApJ*, **815**, 102
- Freiburghaus, C., Rosswog, S., & Thielemann, F. K. 1999, *ApJL*, **525**, L121
- García-Jara, G., Protopapas, P., & Estévez, P. A. 2022, *ApJ*, **935**, 23
- Gheller, C., & Vazza, F. 2022, *MNRAS*, **509**, 990
- Goldstein, A., Veres, P., Burns, E., et al. 2017, *ApJL*, **848**, L14
- Goodfellow, I. J., Pouget-Abadie, J., Mirza, M., et al. 2014, arXiv:1406.2661
- Hotokezaka, K., Kiuchi, K., Kyutoku, K., et al. 2013, *PhRvD*, **87**, 024001
- Hunter, J. D. 2007, *CSE*, **9**, 90
- Jones, E., Do, T., Boscoe, B., et al. 2022, arXiv:2202.07121
- Kasen, D., Badnell, N. R., & Barnes, J. 2013, *ApJ*, **774**, 25
- Kasen, D., Fernández, R., & Metzger, B. D. 2015, *MNRAS*, **450**, 1777
- Kasen, D., Metzger, B., Barnes, J., Quataert, E., & Ramirez-Ruiz, E. 2017, *Natur*, **551**, 80
- Kawaguchi, K., Shibata, M., & Tanaka, M. 2020, *ApJ*, **889**, 171
- Kingma, D. P., & Welling, M. 2013, arXiv:1312.6114
- Kingma, D. P., & Welling, M. 2019, *Found. Trends Mach. Learn.*, **12**, 307
- Lamb, G. P., & Kobayashi, S. 2016, *ApJ*, **829**, 112
- Li, C., Zhang, Y., Cui, C., et al. 2022, *MNRAS*, **509**, 2289
- Li, L.-X., & Paczyński, B. 1998, *ApJL*, **507**, L59
- Lipunov, V. M., Gorbvskoy, E., Kornilov, V. G., et al. 2017, *ApJL*, **850**, L1
- Lukošūtė, K., Raaijmakers, G., Doctor, Z., Soares-Santos, M., & Nord, B. 2022, *MNRAS*, **516**, 1137
- Metzger, B. D. 2019, *LRR*, **23**, 1
- Metzger, B. D., & Fernández, R. 2014, *MNRAS*, **441**, 3444
- Metzger, B. D., Martínez-Pinedo, G., Darbha, S., et al. 2010, *MNRAS*, **406**, 2650
- Nakar, E. 2007, *PhR*, **442**, 166
- Nicholl, M., Margalit, B., Schmidt, P., et al. 2021, *MNRAS*, **505**, 3016
- Ntampaka, M., Ho, M., & Nord, B. 2021, arXiv:2111.14566
- Perego, A., Radice, D., & Bernuzzi, S. 2017, *ApJL*, **850**, L37
- Roberts, L. F., Kasen, D., Lee, W. H., & Ramirez-Ruiz, E. 2011, *ApJL*, **736**, L21
- Rosswog, S., Liebendörfer, M., Thielemann, F. K., et al. 1999, *A&A*, **341**, 499
- Ruffert, M., & Janka, H.-T. 2001, *A&A*, **380**, 544
- Rumelhart, D. E., Hinton, G. E., & Williams, R. J. 1986, *Natur*, **323**, 533
- Savchenko, V., Ferrigno, C., Kuulkers, E., et al. 2017, *ApJL*, **848**, L15
- Shen, H., George, D., Huerta, E. A., & Zhao, Z. 2019, in *IEEE Int. Conf. on Acoustics, Speech and Signal Processing (ICASSP 2019)* (Piscataway, NJ: IEEE), 3237
- Sheng, X., Ross, N., & Nicholl, M. 2022, *MNRAS*, **512**, 5580
- Sipőcz, B. M., Connolly, A., & Ivezić, Ž. 2020, *AAS Meeting*, **235**, 109.15
- Soares-Santos, M., Holz, D. E., Annis, J., et al. 2017, *ApJL*, **848**, L16
- Tanaka, M., & Hotokezaka, K. 2013, *ApJ*, **775**, 113
- Tanaka, M., Utsumi, Y., Mazzali, P. A., et al. 2017, *PASJ*, **69**, 102
- Tanvir, N. R., Levan, A. J., González-Fernández, C., et al. 2017, *ApJL*, **848**, L27
- The pandas development team, 2020, pandas-dev/pandas: Pandas v1.3.5, Zenodo, doi:10.5281/zenodo.3509134
- Valenti, S., Sand, D. J., Yang, S., et al. 2017, *ApJL*, **848**, L24
- van Eerten, H. J., & MacFadyen, A. I. 2012, *ApJ*, **751**, 155
- Vander Plas, J., Connolly, A. J., & Ivezić, Z. 2014, *AAS Meeting*, **223**, 253.01
- Villar, V. A., Cowperthwaite, P. S., Berger, E., et al. 2018, *ApJL*, **862**, L11